Journal of Alloys and Compounds 957 (2023) 170444

Contents lists available at ScienceDirect

Journal of Alloys and Compounds

journal homepage: www.elsevier.com/locate/jalcom

Research article

Reduction of carrier density and enhancement of the bulk Rashba spin-orbit coupling strength in Bi_2Te_3/GeTe superlattices

Seong Won Cho [a,b], Young Woong Lee [a,c], Sang Heon Kim [a,d], Seungwu Han [b], Inho Kim [a], Jong-Keuk Park [a], Joon Young Kwak [a], Jaewook Kim [a], YeonJoo Jeong [a], Gyu Weon Hwang [a], Kyeong Seok Lee [a], Seongsik Park [a], Suyoun Lee [a,e,*]

[a] Center for Neuromorphic Engineering, Korea Institute of Science and Technology, Seoul 02792, South Korea
[b] Department of Materials Science and Engineering, Seoul National University, Seoul 08826, South Korea
[c] Department of Physics, Konkuk University, Seoul 05029, South Korea
[d] Department of Materials and Science Engineering, Korea University, Seoul 02841, South Korea
[e] Division of Nano & Information Technology, Korea University of Science and Technology, Daejeon 34316, South Korea

ARTICLE INFO

Article history:
Received 10 January 2023
Received in revised form 22 April 2023
Accepted 3 May 2023
Available online 5 May 2023

Keywords:
Ferroelectric Rashba semiconductor
Rashba effect
Charge compensation
Superlattice
Weak antilocalization

ABSTRACT

Featured with the large Rashba constant ($\alpha_R \sim 4.2$ eVÅ) coupled with the ferroelectricity, GeTe has attracted much interest, proposing novel energy-efficient spintronic devices. However, those approaches are hampered by the high hole density of GeTe around 10^{20}-10^{21} cm^{-3}, which deteriorates both the ferroelectricity and the bulk Rashba effect of GeTe. To solve this problem, we have investigated the superlattices composed of Bi_2Te_3 and GeTe ([BT|GT] SL), the former of which is known as a topological insulator (TI) with typically *n*-type conduction and strong spin-orbit coupling. We have investigated the magnetotransport properties of 25 $[BT_x|GT_y]_z$ SLs with varying thicknesses (x, y: the thickness in the multiples of the unit cell of the respective layer) of each layer and the repetition number (z) systematically. We have observed a minimum carrier density of 5.7×10^{19} cm^{-3} in $[BT_6|GeTe_6]_6$ superlattice sample smaller than that ($\sim 4.4 \times 10^{20}$ cm^{-3}) of GeTe single film by an order. In addition, we have found that some [BT|GT] SLs with reduced carrier density have a larger Rashba constant compared to that of a single GeTe film. This is explained by the change of the spin polarization which can be modulated by the Fermi level in the Rashba band. These results provide a viable way to realize robust ferroelectricity and strong SOC in GeTe-related material systems simultaneously.

1. Introduction

The concept of spintronics has provided the working principles of novel information devices based on rich fundamental physics, for example, memories [1], transistors [2], and oscillators [3]. Nevertheless, the energy efficiency of these devices needs to be improved to replace the current potentiators of information devices. To this end, in second-generation spintronics [4–9], researchers pursue the electrical control of the electron spin through the spin-orbit (SO) coupling [1,10,11]. In this regard, ferroelectric Rashba semiconductors (FeRSCs) [12–17] are intriguing in that they exhibit the bulk Rashba effect originating from spontaneous electric polarization and strong SO coupling. It implies a possibility of controlling the Rashba effect by the ferroelectric polarization, enabling a large reduction in the operation energy [18–21]. As a prototypical FeRSC with a very large Rashba constant ($\alpha_R \sim 4.2$ eV*Å) [22–25], GeTe (GT) has attracted much interest for spintronic applications such as SO torque magnetic random-access memory [26] (SOT-MRAM) and novel non-volatile spintronic memory devices [27].

Since a theoretical prediction of the huge bulk Rashba effect of GT by Di Sante et al. in 2013 [12], it was experimentally verified by optical spectroscopy and electrical measurements [19,22–24,26,28,29]. Nevertheless, the application of GT in spintronic devices is hampered by the high *p*-type carrier density (10^{20}-10^{21} cm^{-3}) of GT. Such prevailing carriers are known to originate from the inevitable Ge vacancies [30–32], and they are infamous for deteriorating the efficiency of ferroelectric switching [18,33–35] and decreasing the intrinsic Rashba effect of GT [36]. Therefore, it is very important to suppress the generation of carriers in GT for the

* Corresponding author at: Center for Neuromorphic Engineering, Korea Institute of Science and Technology, Seoul 02792, South Korea
E-mail address: slee_eels@kist.re.kr (S. Lee).

https://doi.org/10.1016/j.jallcom.2023.170444
0925-8388/

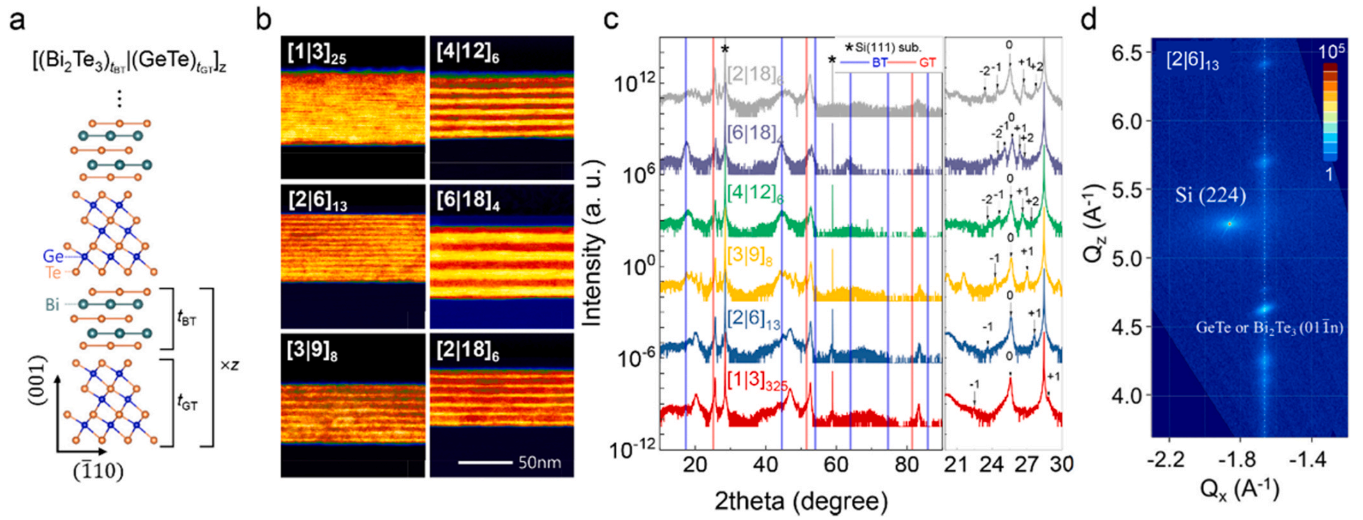

Fig. 1. Structural analysis of the [GT|BT] SLs. (a) Schematic representation of the [BT|GT] SLs. (b) Cross-sectional STEM images of SLs of $[1|3]_{25}$, $[2|6]_{13}$, $[3|9]_8$, $[4|12]_6$, $[6|18]_4$, and $[2|18]_6$, where $[x|y]_z$ notation represents an SL composed of x (u.c.) of the layer BT and y (u.c.) of the GT layer with z representing the repetitions of the layers. (c) (left panel) XRD θ-2θ scans of SLs same as in (b). (right panel) Magnified view in the range from 2theta = 21° to 30° to show satellite peaks clearly. The positions of (000 n) reflection obtained from the 50 nm-thick GT and BT films are indicated by the red and blue vertical lines, respectively. 2θ = 25.106° (0003), 51.558° (0006), and 81.43° (0009) for GT and, 17.37° (0006), 44.51° (00015), 54.035° (00018), 64.05° (00021), 74.66° (00024), and 85.86° (00027) for BT. (d) XRD reciprocal space map (RSM) of the $[2|6]_{13}$ SL around Si (224).

development of highly-efficient spintronic devices utilizing the ferroelectricity coupled Rashba effect.

The most prominent approach for reducing the carrier density of GT has been chemical doping with Sb, Se, Bi, and Mn elements [37–40]. Such approaches revealed the limitation of solubility, leading to a reduction in carrier density by less than an order. In addition, the dopants as defects are likely to deteriorate the periodicity of the lattice and, as a result, weaken the ferroelectricity and the Rashba effect [41]. Indeed, an attempt for the tuning of GeTe's Rashba effect through doping K was reported to lead to a reduction of the Rashba effect as well as the effect being limited to the surface state [42].

In this work, we have investigated superlattice (SL) systems composed of GT and Bi_2Te_3 (BT), because SL can be designed with a high degree of freedom to supply electrons that compensate for holes in GT beyond the solubility limit. Furthermore, the crystalline structure of GT can be preserved with a proper choice of the matching layer. In this regard, BT is chosen as an n-type material that can supply electrons to compensate for holes in GT. Moreover, BT has a hexagonal lattice symmetry with the rhombohedral crystalline structure (R$\bar{3}m$ space group) same as GT (R3m space group) [43,44] and is a well-known three-dimensional topological insulator (TI) with strong SO coupling [45]. We investigate the 25 [BT|GT] SLs by systematically varying the thicknesses of each layer, the period, and the repetition number. We focus on the carrier density and the SO coupling strength of the [BT|GT] SLs depending on the above structural parameters of SL. The SO coupling strength of the SLs is investigated by the analysis of the weak anti-localization [46–49] signal appearing in the magneto-resistance. This investigation will provide information for designing a FeRSC material to have desired properties.

2. Methods

2.1. Film growth and characterization

[BT|GT] SLs were grown with a total thickness of 50 nm by thermal evaporation of atomic sources (Bi, Ge, and Te) on an intrinsic Si (111) substrate at the growth temperature of 250 °C. Before loading into the process chamber, Si (111) substrate was cleaned in the following order: Piranha cleaning, SC1 cleaning, and removal of natural SiO_x in diluted HF solution. After being loaded into the process chamber which has a base pressure of ~10^{-8} Torr, the substrate was preheated to 150 °C for 1 hr to remove residual water on the surface and heated to the growth temperature of 250 °C. Before the SL growth, the buffer layer of 2 nm GT was deposited on Si (111) for reducing the lattice mismatch with BT. The AFM surface image of 3 nm buffer GT on Si (111) substrate is shown in Fig. S4. The fluxes of Bi, Ge, and Te were monitored and controlled by the quartz crystal microbalance (QCM) thickness monitor. The fluxes were set as 0.1, 0.4, and 2.0 Å/s for Bi, Ge, and Te, respectively. By controlling the shutters with the time interval of 5 s, BT and GT were alternately grown. The grown SL films were characterized using XRD (Empyrean, Malvern Panalytical), AFM (XE-70, Park systems), and TEM (TitanTM 80–300, FEI) analysis.

2.2. Carrier transport measurement

The [BT|GT] SLs films were cut into the 5 × 5 mm^2 square and electrical contacts were made at four edges of the samples with indium. The samples were loaded into a commercial cryogen-free cryostat (Cmag Vari.9, Cryomagnetics Inc.) and measured in the temperature range of 1.8 ~ 250 K and the magnetic field range of − 9 ~ 9 T. The longitudinal and the Transversal (Hall) resistances were measured using the conventional Van der Pauw (VdP) method. In the measurement, an SMU (2612 A, Keithley Inc.) as a current source and a nano-voltmeter (2182, Keithley Inc.) as a voltage meter were used.

3. Results and discussion

3.1. Structural characterization of [BT|GT] SLs

The schematic structure of the SL is represented in Fig. 1a. The 25 SLs of $[BT_x|GT_y]_z$ (hereafter denoted as $[x|y]_z$), where x and y denote the thickness of the respective film in the multiples of the unit cell (u.c.) of each layer and z is the repetition number, are grown by the thermal evaporation technique using Bi, Ge, and Te atomic sources. The thicknesses of each layer (t_{BT} and t_{GT} in nm) are varied systematically to be 1, 2, 3, 4, and 6 nm, respectively. The thickness of 1, 2, 3, 4, and 6 nm of BT(GT) layers corresponds to the thickness of 1(3), 2(6), 3(9), 4(12), and 6(18) u.c.'s, respectively. z is set by the total film thickness around 50 nm to exclude the size effect on the transport properties of the SL. We have optimized the growth temperature and the flux of the sources for the high crystalline quality of the grown films (see the "Methods" section for the details of the growth process).

The cross-sectional scanning transmission electron microscope (STEM) images of five symmetric (same thickness for the BT and GT layers) SLs ($[1|3]_{25}$, $[2|6]_{13}$, $[3|9]_{8}$, $[4|12]_{6}$, and $[6|18]_{4}$) and an asymmetric SL ($[2|18]_{6}$) are presented in Fig. 1b to show the structural quality of the investigated SLs. The magnified STEM images are presented in Fig. S1 in the Supporting Information. All SLs show distinctly separated BT (yellow) and GT (red) layers with the intended (t_{BT}, t_{GT}, z) although a slight sign of intermixing is observed for the SLs having a small period.

The out-of-plane (OOP) crystallinity of the SLs is investigated by XRD θ-2θ scans within 10° - 90° range (left panel in Fig. 1c). The reference peak positions of GT (000 n) and BT (000 n), obtained from 50 nm-thick single films of BT and GT, are indicated by blue and red vertical lines, respectively. It is found that GT layers in the SLs have the preferred orientation along the *c*-axis with a slight shift to the higher angle. These peak shifts are associated with the tensile stress exerted by the adjacent BT layers, which is supported by the decreasing trend of the *c*-lattice constant of the GT layer (c_{GT}) with increasing the period (see Fig. S2a in the Supporting Information). On the other hand, the characteristic XRD peaks of the BT layer in SLs become clear for $t_{BT} \geq 3$ nm (left panel in Fig. 1c), for which the peak positions are kept nearly constant independent of BT thickness with the lattice constant same as the 50 nm-thick single BT film (see Fig. S2b in the Supporting Information). It is associated with the two-dimensional (2D) nature of the crystal structure of BT. In addition, Fig. 1c (right panel) shows the SL satellite peaks [50] around GT (0003), which guarantees the well-grown epilayer with the coherent periodicity of SLs. From the distance between the main peak and the satellite peak, the period of $[1|3]_{25}$, $[2|6]_{13}$, $[3|9]_{8}$, $[4|12]_{6}$, $[6|18]_{4}$, and $[2|18]_{6}$ SLs are calculated to be 2.9, 4.5, 6.6, 9.2, 14.2, 8.2 nm, respectively, which agree with the designed period values within an error of at most 10%.

Fig. 1d shows the XRD reciprocal space map (RSM) of $[2|6]_{13}$ SL as a representative example (for the others, see Fig. S3 in the Supporting Information). The peaks are only observed at Q_x ~1.67 Å^{-1}, which correspond to $(01\bar{1}n)$ of GT or BT and implies the well-ordered in-plane crystallinity. The stretched peaks in the Q_x direction suggest a strain effect due to ~ 5% in-plane lattice mismatch between GT and BT.

The morphology of the SL structures is investigated by using the atomic force microscope (AFM, see Fig. S4 in the Supporting Information) to find a quite flat surface of the SLs with the root-mean-square (RMS) roughness of 0.3 ~ 0.5 nm.

3.2. Basic carrier transport properties of [BT|GT] SLs

The basic carrier transport properties of [BT|GT] SLs have been investigated by measuring the longitudinal and transversal resistance with varying temperatures and magnetic fields (see Fig. S5-S7 in the Supporting Information). Fig. 2a-c shows the resistivity, carrier density, and carrier mobility at 1.8 K as a function of t_{BT} and t_{GT}, respectively. In Fig. 2a, note that the resistivity changes drastically from 0.3 mΩcm to 3.8 mΩcm as the composition changes from $[1|6]_{12}$ to $[3|3]_{13}$ with a composition-dependence similar to that of the carrier density (Fig. 2b). The maximal carrier compensation is acquired in the case of $t_{BT}/t_{GT} \approx 3$, leading to the crossover of the carrier type across that region (the white region in Fig. 2b). It is consistent with the fact that the hole density (4.36×10^{20} cm^{-3}) in the GT layer is ~ 3 times larger than the electron density (1.49×10^{20} cm^{-3}) in the BT layer. For the investigated SLs, the minimum carrier density is observed to be ~ 5.7×10^{19} cm^{-3} in $[6|6]_{6}$ SL, reduced by about an order compared to the single GT film.

The carrier mobility (μ_{SL}) of SLs at $T = 1.8$ K is presented in Fig. 2c, where μ_{SL} tends to increase as t_{GT} decreases and t_{BT} increases. It is intriguing to find that the colormap of μ_{SL} resembles that of n_{SL}, implying that the interaction between carriers plays an important role in carrier transport in SL. In addition, the SL seems to play as a whole conductor, not as a simple sum of separated GT and BT channels, which is supported by the quite linear dependence of the transversal resistance (R_{xy}) on the external magnetic field (H) as shown in Fig. S7 in the Supporting Information. These observations validate our idea in this work, which assumes the carriers in the GT layer can be compensated in the SL with an appropriate design of SL parameters.

Fig. 2d shows $|n|$ as a function of z for various values of t_{BT}/t_{GT}. Note that $|n|$ tends to increase as z increases, which implies that the alloying at the interface rarely contributes to the carrier compensation effect, because the alloying volume is proportional to z. Instead, the carrier compensation effect can be explained through the charge transfer effect between BT- and GT- domains, in which the area of the interface is less important. In Figs. 2e and 2f, $|n|$ is plotted as a function of the period ($t_{BT} + t_{GT}$) of an SL and t_{BT}, respectively, for various t_{BT}/t_{GT}. In Fig. 2f, it is interesting to find that the $|n|$ vs. t_{BT} curve shows a universal behavior independent of t_{BT}/t_{GT}. It can be explained in terms of the depletion width at the BT side. In detail, due to the difference in the work functions (ϕ_{GT} ~ 4.8 eV, ϕ_{BT} ~ 4.5 eV) [18,51], GT and BT layers transfer major carriers to each other, forming a depletion region at each side of the interface. In a *p-n* junction, the depletion width ($w_{n(p)}$) is given by $w_{n(p)} = \sqrt{\frac{2\varepsilon\Delta\phi}{q}\frac{N_{a(d)}}{N_{d(a)}}\frac{1}{N_a+N_d}}$ [52], where ε, q, and $\Delta\phi$ are the dielectric constant of the medium, the electron charge, and the built-in voltage, respectively. N_a and N_d are the density of acceptor and donor atoms, which are assumed to be p_{GT} (4.3×10^{20} cm^{-3}) and n_{BT} (1.5×10^{20} cm^{-3}), respectively. In addition, from the assumption of $\varepsilon_{BT} = 32$ [53] and $\varepsilon_{GT} = 30$ [54], the w_{BT} and w_{GT} are calculated to be ~ 2 nm and ~ 0.7 nm, respectively, indicating that the BT layer thicker than 2 nm is required for sufficient charges to be transferred into GT layer. Conversely, the BT layer with a thickness under 2 nm leads to the increase in $|n|$ as observed in Fig. 2f. In addition, the characteristic decay length of the phenomenological exponential dependence of $|n|$ on t_{BT} (dashed line in Fig. 2f) is estimated around 1 nm, which means the 86% reduction of $|n|$ when $t_{BT} = w_{BT}$, supporting the model.

3.3. Rashba constant of [BT|GT] SLs

For investigating Rashba SO coupling of [BT|GT] SLs, we have analyzed the magnetoresistance (MR) vs. H curve that shows the weak antilocalization (WAL)-induced cusp whose magnitude depends on the spin-orbit coupling [55–57]. The representative MR vs. H curves of [BT|GT] SLs (t_{BT} = 1 nm and t_{GT} = 1, 2, 3, 4, and 6 nm) at $T = 1.8$ K are presented in Fig. 3a, where the cusp near $H = 0$ is observed clearly with its saliency depending on the composition of the SL (see Fig. S8 and Fig. S9 in the Supporting Information for $MR(H)$ curves of the other SL samples and the typical temperature-dependence of the MR(H) curve, respectively).

For the quantitative analysis of the WAL, the $MR(H)$ is decomposed into the WAL-induced MR (MR_{wal}) and the classical one (MR_{ord}) (for the details of this process, see Fig. S10 in the Supporting Information). Fig. 3b-f shows the $MR_{wal}(H)$ in which the cusps are more emphasized. The functional form of $MR_{wal}(H)$ depends on the spin relaxation mechanisms (Elliot-Yafet (EY) [58,59] or D′yakonov-Perel (DP) [60]) and the dimensionality of the transport channel. Among the models, the Fukuyama-Hoshino (FH) model assumes the three-dimensional (3D) transport whose validity in [BT|GT] SLs is

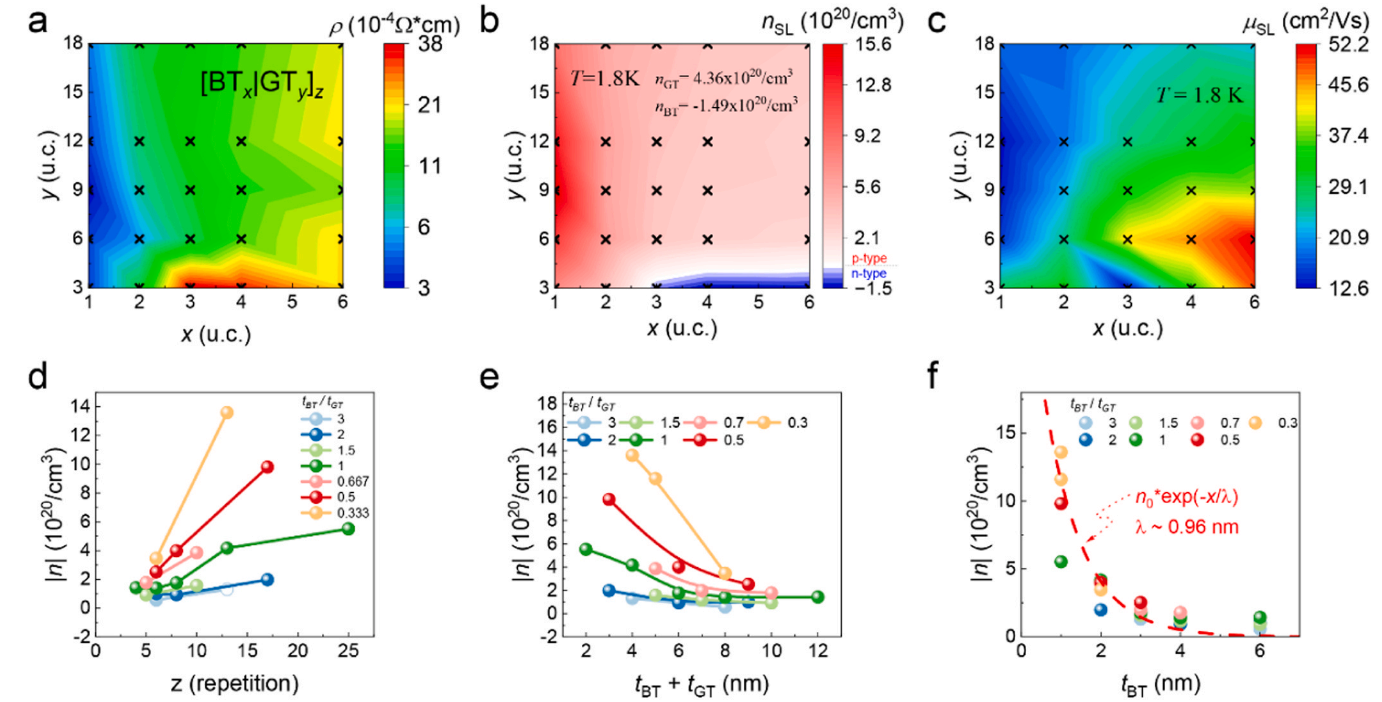

Fig. 2. Basic carrier transport of $[BT_x|GT_y]_z$ SLs. (a)-(c) Color maps for ρ (a), n (b), and μ (c) in the plane of (x, y), where × symbols represent the experimental data points. (d) $|n|$ vs. z, (e) $|n|$ vs. SL period ($t_{BT}+t_{GT}$) and (f) $|n|$ vs. t_{BT} according to the various t_{BT}/t_{GT}.

justified by the charge transfer (Fig. 2d) and the DP spin relaxation mechanism which covers the Rashba system.

The FH model [46,56,61–64] is expressed by the following equations:

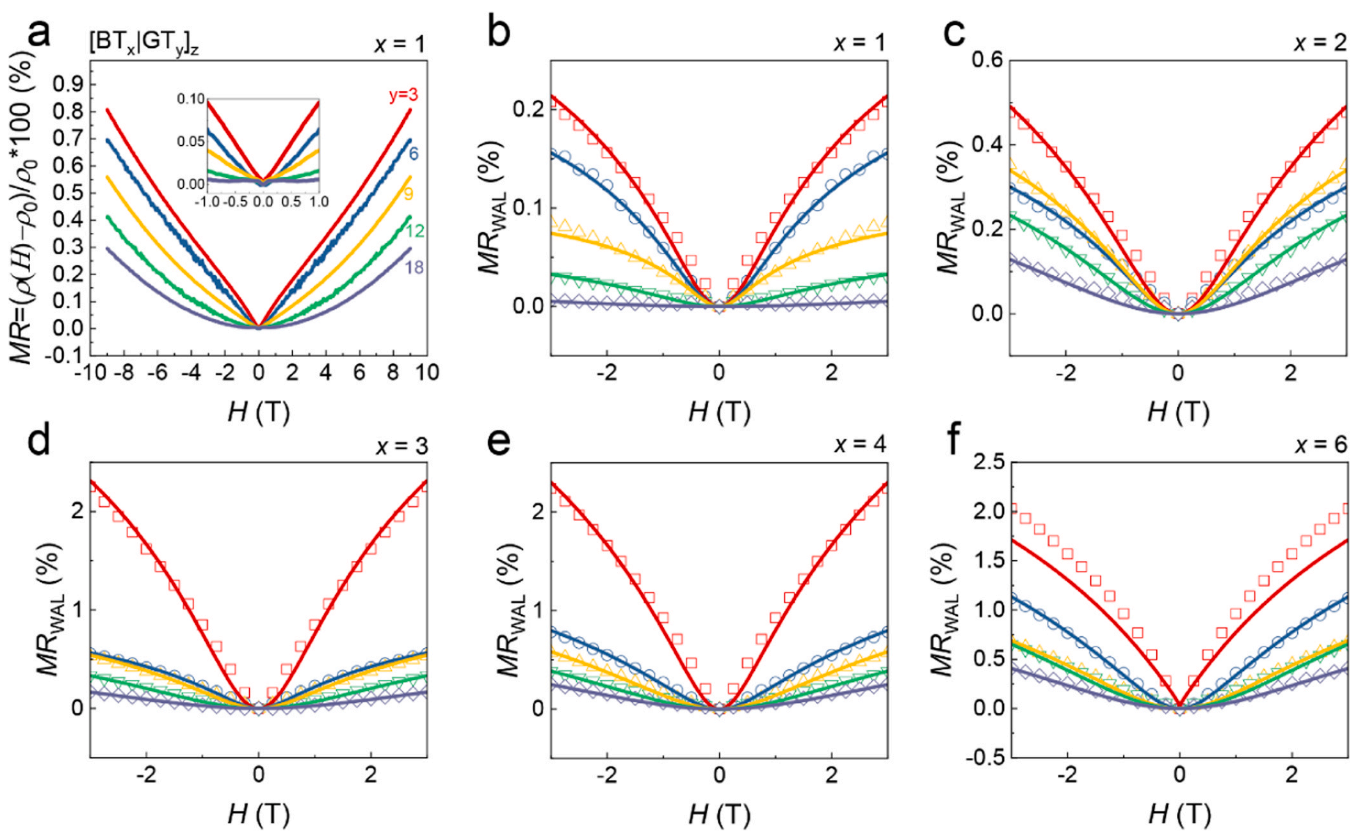

Fig. 3. The analysis of the weak anti-localization (WAL). (a) Representative $MR(H)$ curves before subtracting the ordinary $MR(H)$. (b)-(f) $MR_{WAL}(H)$ curves (open symbol, see Fig. S10 for the details of the extraction process) and the fitting curves with FH model (lines) of $[BT_x|GT_y]_z$ SLs (y = 3, 6, 9, 12, and 18 u.c.) as x = 1 u.c. (a), 2 u.c. (b), 3 u.c. (c), 4 u.c. (d), and 6 u.c. (e). The measurements are performed at T = 1.8 K and the color code is the same in all the plots.

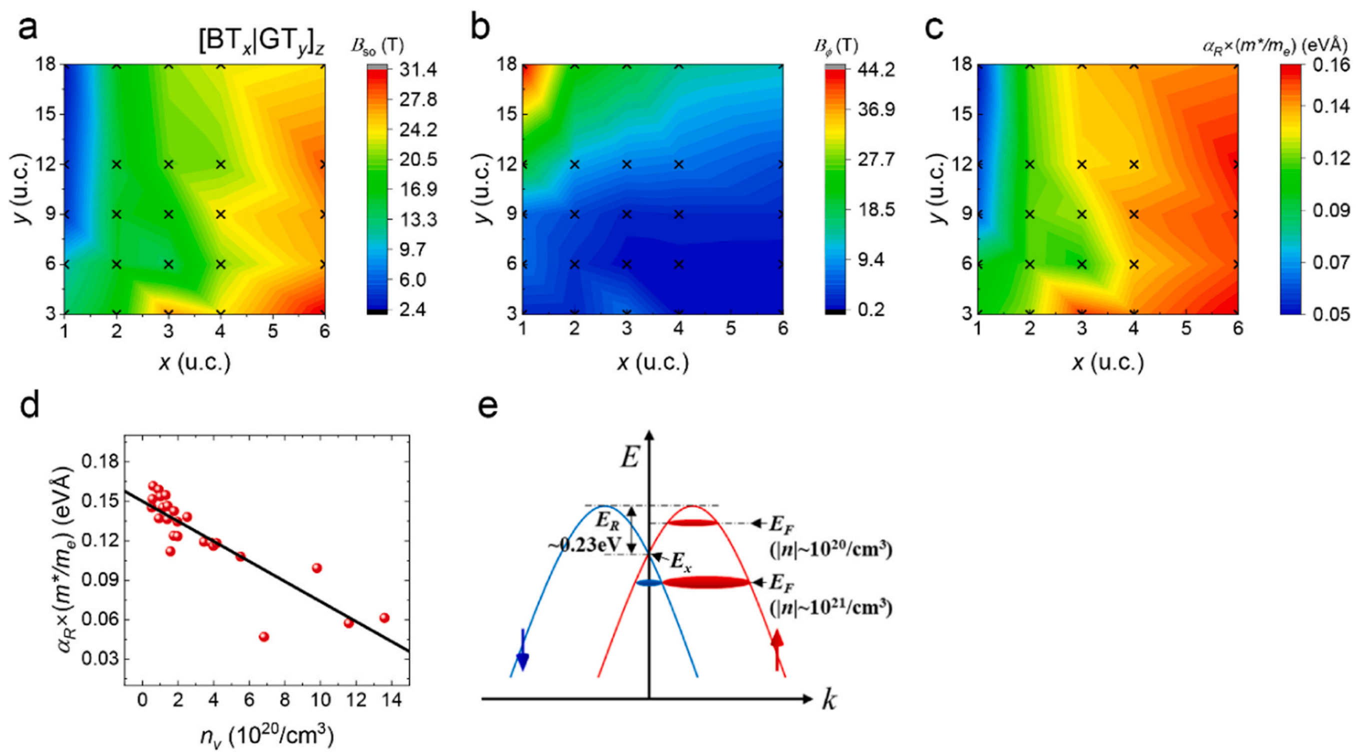

Fig. 4. Spin-orbit coupling strength of $[BT_x|GT_y]_z$ SLs, (a)-(c) The color map for B_{so} (a), B_ϕ (b), and $\alpha_R \times m^*/m_e$ (c), which are obtained from the fitting the *MR* vs. *H* curves in Eq. 3 to Eq. (1) (see the main text), in (*x*, *y*)-plane. × symbols represent the experimental data points. (d) $\alpha_R \times m^*/m_e$ as a function of carrier density (red circle) with a linear fitting curve (black line). (e) The schematic cartoon for showing the spin polarization according to the position of the Fermi level in the Rashba band.

$$MR_{WAL}(H) = 100\rho_0\frac{e^2}{2\pi^2\hbar}\sqrt{\frac{eH}{\hbar}}\left(\frac{1}{2\sqrt{1-\gamma}}\left[f_3\left(\frac{H}{B_-}\right)-f_3\left(\frac{H}{B_+}\right)\right]-f_3\left(\frac{H}{B_2}\right)-\sqrt{\frac{4B_{so}}{3H}}\left[\frac{1}{\sqrt{1-\gamma}}\left(\sqrt{t_+}-\sqrt{t_-}\right)+\sqrt{t}-\sqrt{t+1}\right]\right) \quad (1)$$

$$f_3(y) = \sum_{n=0}^{\infty}\left[2\left(n+1+\frac{1}{y}\right)^{\frac{1}{2}} - 2\left(n+\frac{1}{y}\right)^{\frac{1}{2}} - \left(n+\frac{1}{2}+\frac{1}{y}\right)^{-\frac{1}{2}}\right] \quad (2)$$

where

$$\gamma = \left[\frac{3g^*\mu_B H}{4eD(2B_{so}-B_0)}\right]^2 \quad (3)$$

$$B_\pm = B_\phi + \frac{1}{3}(2B_{so}-B_0)(1\pm\sqrt{1-\gamma}) \quad (4)$$

$$B_\phi = B_i + B_0 \quad (5)$$

$$B_2 = B_i + \frac{1}{3}B_0 + \frac{4}{3}B_{so} \quad (6)$$

$$t = \frac{3B_\phi}{2(2B_{so}-B_0)} \quad (7)$$

$$t_\pm = t + \frac{1}{2}(1\pm\sqrt{1-\gamma}) \quad (8)$$

Here, $\hbar$, g^*, μ_B, and D are the reduced Planck constant ($h/2\pi$), the effective Landé g factor, Bohr magneton, and the diffusion coefficient of the electron in the SL, respectively. B_α ($\alpha = i$, 0, so, and ϕ) is the characteristic magnetic field representing the inelastic scattering ($\alpha = i$), the remanent which means the dephasing field at $T \approx 0$ ($\alpha = 0$), the SO interaction (α = so), and the dephasing ($\alpha = \phi$), respectively. Among these four B_αs, only B_ϕ and B_{so} are set as two independent fitting parameters with a constraint given by Eq. (5) and an assumption of $B_0 = 0$ [63]. By fitting Eq. (1) to the data, B_ϕ and B_{so} are estimated with assumptions of $g^* = 0.3$ [65] and $D = \mu k_B T/e$ (where, μ = the carrier mobility, k_B = the Boltzmann constant). In Fig. 3(b) ~ (f), the solid lines represent the fitting curves showing that the *MR* (*H*) of [BT|GT] SLs are well described by the FH model except for the $[6|3]_7$. The discrepancy in the $[6|3]_7$ might be due to the relatively large portion of BT, where the carrier transport is likely to have 2D nature and the spin relaxation is dominated by the EY mechanism, deviating from the 3D nature and DP mechanism assumed in the FH model.

Figs. 4a and 4b show the extracted fitting parameters, B_ϕ and B_{so} in $[BT_x|GT_y]_z$, as the color maps in (*x*, *y*)-plane. It is observed that B_{so} increases from 2 T up to 31 T as *x*/*y* increases showing a trend similar to n_{SL} (Fig. 2b). It seems to imply that there is a correlation between n_{SL} and B_{so}, which will be discussed in the later part. On the other hand, the observed increase in B_ϕ with increasing *y* implies that the dephasing scatterings become dominant with the Ge vacancies. This is supported by the observation of B_ϕ inversely proportional to μ (see Fig. S11(a) in the Supporting Information). In contrast, the B_{so} is found to increase as μ increases (see Fig. S11(b) in the Supporting Information), supporting the spin relaxation by the DP mechanism [66]. When the spin relaxation is governed by the DP mechanism, the Rashba constant (α_R) can be calculated from B_{so} by using the relationship of $\alpha_R = \frac{e\hbar^3 B_{so}}{m^*}$, where m^* is the effective mass of the electron [57,67]. Fig. 4c shows the calculated $\alpha_R(m^*/m_e)$ as a color map in space of t_{BT}-t_{GT}. In addition, the same quantity is plotted as a function of *n* in Fig. 4d, in which a linear relationship between α_R and *n* with a negative slope is observed. For $[1|18]_7$ SL, α_R is estimated around 0.31 ~ 2.14 eVÅ with $m^* = 0.022$ ~ 0.15 [65,68], much lower than the known value of 4.2 eVÅ of GT. Such a low α_R in GT-rich SLs can be associated with their large carrier density. Indeed, in the recent calculation of the spin Hall conductivity of GT, a relatively small spin Hall angle of only 0.01 which is reduced due to their large carrier density was predicted [36]. Nevertheless, α_R of SLs is found to increase up to 1.1 ~ 7.4 eVÅ as t_{BT} increases. Such an increase in α_R with increasing t_{BT} can be explained in terms of the strong SO coupling in the BT layer. Proximity-induced SOC crossing the Van der Waals (VdW) gap can endow strong SOC in the BT layer to the GT layer [69,70]. However, the observed maximum α_R of 7.4 eVÅ is significantly larger than the reported values of 0.1–1 eVÅ in BT, requiring alternative scenarios to explain it. Fermi level (E_F) tuning confirmed by carrier density variation can effectively explain the observed variation of α_R in SL. Fig. 4e shows a schematic electronic band structure of a [BT|GT] SL. When the BT layer is thin, hole carriers are abundant positioning E_F lower than the crossing point (E_x) of the spin-up band and the spin-down band. In that case, the carriers with a specific sign of momentum (for example, $+k_x$ or $-k_x$ momentum) are not fully spin-polarized lowering the effective Rashba constant ($\alpha_{R,eff}$). As t_{BT} increases, n decreases making E_F higher than E_x, in which the spins of the carriers are fully polarized with being locked to their momentum. As a result, a large $\alpha_{R,eff}$ is observed, consistent with our observation [71].

4. Conclusions

We have systematically investigated the $[BT_x|GT_y]_z$ SLs aiming at achieving robust ferroelectricity and strong SO coupling simultaneously by suppressing the generation of carriers prevalent in GT. From the analysis of the basic transport properties of SLs, we have found that the carrier density has its minimum when $t_{BT} \approx 3 \times t_{GT}$ with the value lower by orders of magnitude compared to that of a single GT film. Such a condition of the minimal $|n|$ is determined by the relationship between bulk carrier densities of GT and BT layers. With this composition, it is found that the strength of the Rashba effect does not deteriorate, but rather increases in the [BT|GT] SL structure. Therefore, these results provide a viable way to realize robust ferroelectricity and strong SOC in GeTe-related material systems simultaneously. In addition, we believe that our results provide useful information for developing thermoelectric materials with a high figure of merit by reducing the carrier density.

Credit authorship contribution statement

Seong Won Cho: Validation, Formal analysis, Investigation, Writing – original draft. **Young Woong Lee:** Validation, Resources. **Sang Heon Kim:** Validation, Data curation. **Seungwu Han:** Resources, Writing – review & editing. **Inho Kim:** Writing – review & editing. **Jong-Keuk Park:** Writing – review & editing. **Joon Young Kwak:** Writing – review & editing. **Jaewook Kim:** Writing – review & editing, Validation. **YeonJoo Jeong:** Writing - Review & Editing. **Gyu Weon Hwang:** Writing – review & editing. **Kyeong Seok Lee:** Writing – review & editing. **Seongsik Park:** Writing – review & editing, Validation. **Suyoun Lee:** Conceptualization, Writing – original draft, Writing – review & editing, Supervision, Project administration, Funding acquisition.

Data Availability

No data was used for the research described in the article.

Declaration of Competing Interest

The authors declare that they have no known competing financial interests or personal relationships that could have appeared to influence the work reported in this paper.

Acknowledgments

This work was supported by the Korea Institute of Science and Technology (KIST) through 2E32260 and by the National Research Foundation program through NRF-2021M3F3A2A03017782, NRF-2021M3F3A2A01037814, NRF-2021R1A2C3011450, and NRF-2021M3F3A2A01037738.

Appendix A. Supporting information

Supplementary data associated with this article can be found in the online version at doi:10.1016/j.jallcom.2023.170444.

References

[1] J. Puebla, J. Kim, K. Kondou, Y. Otani, Commun. Mater. 1 (2020) 24.
[2] S. Datta, Nat. Electron 1 (2018) 604.
[3] B. Dieny, et al., Nat. Electron. 3 (2020) 446.
[4] A. Hirohata, K. Yamada, Y. Nakatani, I.-L. Prejbeanu, B. Diény, P. Pirro, B. Hillebrands, J. Magn. Magn. Mater. 509 (2020) 166711.
[5] M. He, H. Sun, Q.L. He, Front. Phys. 14 (2019) 43401.
[6] S.-H. Yang, R. Naaman, Y. Paltiel, S.S.P. Parkin, Nat. Rev. Phys. 3 (2021) 328.
[7] Q.L. He, T.L. Hughes, N.P. Armitage, Y. Tokura, K.L. Wang, Nat. Mater. 21 (2021) 15.
[8] D.D. Awschalom, M.E. Flatté, Nat. Phys. 3 (2007) 153.
[9] Handbook of Spintronics (Springer Dordrecht, 1 edn.).
[10] Z. Guo, J. Yin, Y. Bai, D. Zhu, K. Shi, G. Wang, K. Cao, and W. Zhao, Proceedings of the IEEE **109**, 1398 (2021).
[11] A. Hoffmann, S.D. Bader, Phys. Rev. Appl. 4 (2015) 047001.
[12] D. Di Sante, P. Barone, R. Bertacco, S. Picozzi, Adv. Mater. 25 (2013) 509.
[13] J.E. Boschker, R. Wang, R. Calarco, CrystEngComm 19 (2017) 5324.
[14] K. Ishizaka, et al., Nat. Mater. 10 (2011) 521.
[15] M.S. Bahramy, R. Arita, N. Nagaosa, Phys. Rev. B 84 (2011) 041202.
[16] S. Picozzi, Front. Phys. 2 (2014) 10.
[17] H. Murakawa, M.S. Bahramy, M. Tokunaga, Y. Kohama, C. Bell, Y. Kaneko, N. Nagaosa, H.Y. Hwang, Y. Tokura, Science 342 (2013) 1490.
[18] S. Varotto, et al., Nat. Electron. 4 (2021) 740.
[19] J. Krempaský, et al., J. Phys. Chem. Solids 128 (2019) 237.
[20] Y.-H. Meng, W. Bai, H. Gao, S.-J. Gong, J.-Q. Wang, C.-G. Duan, J.-H. Chu, Nanoscale 9 (2017) 17957.
[21] W. Zhang, Z. Teng, H. Zeng, H. Zhang, J. Železný, W. Zhang, Phys. Status Solidi (b) 257 (2020) 2000143.
[22] J. Krempaský, et al., Phys. Rev. Res. 2 (2020) 013107.
[23] J. Krempaský, et al., Phys. Rev. B 94 (2016) 205111.
[24] J. Krempaský, et al., Nat. Commun. 7 (2016) 13071.
[25] H.J. Elmers, et al., Phys. Rev. B 94 (2016) 201403.
[26] J. Jeon, et al., npg Asia Mater. 13 (2021) 76.
[27] C. Rinaldi, et al., Nano Lett. 18 (2018) 2751.
[28] H. Przybylińska, G. Springholz, R.T. Lechner, M. Hassan, M. Wegscheider, W. Jantsch, G. Bauer, Phys. Rev. Lett. 112 (2014) 047202.
[29] C. Rinaldi, et al., APL Mater. 4 (2016) 032501.
[30] A. Edwards, A. Pineda, P. Schultz, M. Martin, A. Thompson, H. Hjalmarson, C. Umrigar, Phys. Rev. B 73 (2006) 045210.
[31] V.L. Deringer, M. Lumeij, R. Dronskowski, 116 (2012) 15801.
[32] D.H. Damon, M.S. Lubell, R. Mazelsky, 28 (1967) 520.
[33] A.V. Kolobov, D.J. Kim, A. Giussani, P. Fons, J. Tominaga, R. Calarco, A. Gruverman, 2 (2014) 066101.
[34] P. Nukala, M. Ren, R. Agarwal, J. Berger, G. Liu, A.T.C. Johnson, R. Agarwal, Nat. Commun. 8 (2017) 15033.
[35] K. Jeong, H. Lee, C. Lee, L.H. Wook, H. Kim, E. Lee, M.-H. Cho, Appl. Mater. Today 24 (2021) 101122.
[36] H. Wang, P. Gopal, S. Picozzi, S. Curtarolo, M. Buongiorno Nardelli, J. Sławińska, npj Comput. Mater. 6 (2020) 7.
[37] N. Madar, T. Givon, D. Mogilyansky, Y. Gelbstein, J. Appl. Phys. 120 (2016) 035102.
[38] J. Li, X. Zhang, S. Lin, Z. Chen, Y. Pei, Chem. Mater. 29 (2017) 605.
[39] Z. Liu et al., Proceedings of the National Academy of Sciences **115**, 5332 (2018).
[40] E. Nshimyimana, X. Su, H. Xie, W. Liu, R. Deng, T. Luo, Y. Yan, X. Tang, Sci. Bull. 63 (2018) 717.
[41] A.I. Lebedev, I.A. Sluchinskaya, V.N. Demin, I.H. Munro, Phase Transit. 60 (1997) 67.
[42] H. Ryu, et al., Phys. Rev. B 103 (2021) 245113.
[43] J. Krumrain, G. Mussler, S. Borisova, T. Stoica, L. Plucinski, C.M. Schneider, D. Grützmacher, J. Cryst. Growth 324 (2011) 115.
[44] H. Zhang, D.T. Yimam, S. De Graaf, J. Momand, P.A. Vermeulen, Y. Wei, B. Noheda, B.J. Kooi, ACS Nano 15 (2021) 2869.
[45] Y.L. Chen, et al., Science 325 (2009) 178.
[46] H. Fukuyama, K. Hoshino, J. Phys. Soc. Jpn. 50 (1981) 2131.
[47] S.W. Cho, K.-C. Kim, S.K. Kim, B.-K. Cheong, J.-S. Kim, S. Lee, J. Alloy. Compd. 723 (2017) 942.
[48] S.W. Cho, M. Lee, S. Woo, K. Yim, S. Han, W.S. Choi, S. Lee, Sci. Rep. 8 (2018) 5739.
[49] M. Lee, S.W. Cho, Y. Yi, S. Lee, J. Alloy. Compd. 800 (2019) 81.

[50] S. Cecchi, E. Zallo, J. Momand, R. Wang, B.J. Kooi, M.A. Verheijen, R. Calarco, APL Mater. 5 (2017) 026107.
[51] Y. Liu, E. Mu, Z. Wu, Z. Che, F. Sun, X. Fu, F. Wang, X. Wang, Z. Hu, Nano Converg. 7 (2020) 8.
[52] Photovoltaics Education Website, ⟨www.pveducation.org⟩.
[53] B. Mohamed, M. Allel, D. Bendouma, B. Miloud, Mater. Res. 21 (2017) 1.
[54] L. Guarneri, et al., Adv. Mater. 33 (2021) 2102356.
[55] H. Nakamura, D. Huang, J. Merz, E. Khalaf, P. Ostrovsky, A. Yaresko, D. Samal, H. Takagi, Nat. Commun. 11 (2020) 1161.
[56] J.J. Lin, J.P. Bird, J. Phys.: Condens. Matter 14 (2002) R501.
[57] T. Koga, J. Nitta, T. Akazaki, H. Takayanagi, Phys. Rev. Lett. 89 (2002) 046801.
[58] R. Elliott, Phys. Rev. 96 (1954) 280.
[59] Y. Yafet, Solid state physics, Elsevier, 1963, p. 1.
[60] M. D′yakonov, V. Perel, Zh. Eksp. Teor. Fiz. 65 (1973) 362.
[61] Y. Nakazawa, M. Uchida, S. Nishihaya, M. Ohno, S. Sato, M. Kawasaki, Phys. Rev. B 103 (2021) 045109.
[62] E.R. Viana, G.M. Ribeiro, A.G.D. Oliveira, M.L. Peres, R.M. Rubinger, C.P.L. Rubinger, Mater. Res. 15 (2012) 530.
[63] S.T. Lim, L. Hui, J.F. Bi, K.L. Teo, J. Appl. Phys. 110 (2011) 113916.
[64] M.L. Peres, V.A. Chitta, N.F. Oliveira, D.K. Maude, P.H.O. Rappl, A.Y. Ueta, E. Abramof, Phys. Rev. B 79 (2009) 085309.
[65] D. Huang, G. Gumbs, M. Lanius, A.R. Jalil, P. Schüffelgen, G. Mussler, D. Grützmacher, V. Narayan, Phys. Lett. A 411 (2021) 127550.
[66] A.D. Caviglia, M. Gabay, S. Gariglio, N. Reyren, C. Cancellieri, J.M. Triscone, Phys. Rev. Lett. 104 (2010) 126803.
[67] S. Takasuna, J. Shiogai, S. Matsuzaka, M. Kohda, Y. Oyama, J. Nitta, Phys. Rev. B 96 (2017) 161303.
[68] X. Chen, D. Parker, D.J. Singh, Sci. Rep. 3 (2013) 3168.
[69] W. Zhu, et al., Adv. Funct. Mater. 32 (2022) 2108953.
[70] H. Wang, et al., ACS Nano 14 (2020) 10045.
[71] P.C. Verpoort, V. Narayan, J. Phys.: Condens. Matter 32 (2020) 355704.